

HOW WELL CAN WEAK LENSING MEASURE THE MASS OF GALAXY CLUSTERS?

Jun-Mein Wu¹, Keiichi Umetsu², Chia-Hung Chien¹, Tzihong Chiueh¹

ABSTRACT

The technique of weak-lensing aperture mass densitometry, so called the ζ -statistic, has recently been popular in actual observations for measurement of individual cluster mass. It has however been anticipated that the line-of-sight projection by foreground and background matter can adversely affect the cluster mass determination with not only substantial error dispersion but also a sizable positive systematic bias. Additionally, the finite number of background galaxies even at a reasonable observing depth can also introduce Poisson noise to the mass estimate. In this paper, we quantitatively investigate the degree of errors separately contributed by the two sources to the mass determination of those galaxy clusters with $M_{200} > 10^{14} M_{\odot}$. We find that the aperture mass of ζ -statistic turns out to be a mass estimator of much reduced systematic bias, due to the cancellation by the positively biased local background mass sheet. However, the error dispersion of M_{200} arising from both projection effect and Poisson noise is found to be still sizable (40% – 90%), even for the shear-selected, clean sample where multiple clusters located within a suitable projected aperture are removed. We also investigate how to remedy this large-error problem in weak lensing measurements, and propose a plausible alternative mass estimator, $M(< \theta_{1000})$, an aperture mass measured within about half the virial radius. The aperture mass $M(< \theta_{1000})$ is free of bias and has a substantially reduced error dispersion, 39% for the worst case of high- z , low-mass clusters, that can be smaller than the error dispersion of M_{200} as much as a factor 3.

Subject headings: cosmology: theory — dark matter — galaxies: clusters: general — gravitational lensing

¹Department of Physics, National Taiwan University, Wenshan Chiu, Taipei 116, Taiwan

²Institute of Astronomy and Astrophysics, Academia Sinica, P. O. Box 23-141, Taipei 106, Taiwan, Republic of China

1. INTRODUCTION

The mass function of galaxy clusters has long been recognized as the most convenient and important indicator for probing the evolution of structure formation, thereby helping determine the cosmological parameters. In addition, the cluster halo mass, when combined with the cluster gas mass via the Sunyaev-Zel'dovich effect, provides the opportunity for probing the cluster baryon fraction (Umetsu, et al. 2005). Conventional techniques, such as measuring the velocity dispersion of gravitationally bound galaxies and the X-ray emission profile, have long been employed to measure the cluster mass, assuming cluster galaxies and X-ray emitting plasmas to be dynamically relaxed within the cluster gravitational potential.

On the other hand, the new technique of mass measurement through weak gravitational lensing has been gaining popularity in recent years, with the advantage of not having to assume the dynamical equilibrium in the cluster (e.g., Umetsu, Tada, & Futamase 1999; Bartelmann & Schneider 2001; Schneider 2005). This methodology was first pioneered by Tyson et al. (1990). Various refined techniques for the weak-lensing mass determination were later proposed by several groups (Fahlman et al. 1994; Kaiser 1995; Bartelmann 1995; Seitz & Schneider 1996; Squires & Kaiser 1996; Broadhurst, Takada, Umetsu et al. 2005).

Among these techniques, the ζ -statistic was particularly devised to measure the lens mass directly from the tangential component of local gravitational image distortions without involving a non-local mass reconstruction (Fahlman et al. 1994; Kaiser 1995). Schneider (1996) extended the ζ -statistic by generalizing its kernel, which allows one to define an optimal measure for the detection of mass concentrations, and this aperture mass technique has been applied to deep optical imaging data to search for clusters (e.g., Erben et al. 2000; Umetsu & Futamase 2000; Wittman et al. 2001, 2003; Miyazaki et al. 2002; Dahle et al. 2003; Hetterscheidt et al. 2005; Schirmer et al. 2006). King et al. (2001) investigated the cluster mass measurement influenced by interior substructures, and found the measured mass as accurate as within 10%. Clowe et al. (2004) studied the effect of asphericity on the cluster mass determination, and concluded, under the assumption of an NFW profile, that the asphericity effect generally changes the mass estimate by 5% to 10%.

In addition, several authors have compared the weak-lensing mass with the mass determined by the galaxy kinematics and X-ray observations. Reblinsky & Bartelmann (1999) concluded that the mass estimates using ζ -statistic are significantly more accurate than those obtained from the galaxy kinematics. Ettori & Lombardi (2003) studied the mass distribution of the rich cluster MS 1008.1-1224 at $z = 0.302$ based on *Chandra* X-ray and FORS1-VLT multicolor-imaging data, and they found that the two mass profiles obtained from X-ray and weak-lensing analyses up to $550h^{-1}$ kpc are consistent with each other within 1σ uncertainty.

Irgens et al. (2002), assuming a singular isothermal sphere model for the cluster mass profile, compared spectroscopic velocity dispersions, σ_p , of 13 X-ray luminous clusters around $z \sim 0.3$ with σ_{WL} of these clusters determined by weak-lensing tangential shear measurements out to the cluster virial radius. It was found that among all, two clusters are in strong discrepancy, with $\sigma_{WL} > 2\sigma_p$ and $\sigma_{WL} \approx 2\sigma_p$, whereas the rest are in fair agreement, with $\langle \sigma_p / \sigma_{WL} \rangle \approx 1$. Though these exceptional clusters may be in dynamical non-equilibrium, another possibility may arise from the projection effects of other mass concentrations (Cen 1997; Reblinsky & Bartelmann 1999; White, van Waerbeke, & mackey 2002; Padmanabhan, Seljak, & Pen 2003; Hamana, Takada, & Yoshida 2004; Henawi & Spergel 2005) and/or local filamentary structures (Metzler et al. 1999; Metzler, White, & Loken 2001) along the line-of-sight. Using N -body simulations White et al. (2002) studied the completeness and efficiency of weak-lensing cluster surveys on the basis of their *mass-selected* mock cluster sample and found that the line-of-sight projection effects can be quite serious due to the broad lensing kernel. In the cluster mass estimate based on the convergence map, they found a positive bias of $\sim 20 - 30\%$ with a substantially larger error dispersion that can even occasionally yield negative lens masses. Metzler et al. (1999; 2001) studied the projection effects on weak-lensing mass estimates for massive clusters caused by the local large-scale filamentary structures. Including the projection effects from local matter within a sphere of $128h^{-1}\text{Mpc}$ radius, they found the lensing convergence maps to yield an positive mass bias of $\sim 30\%$ and the mass error dispersion of ~ 0.3 for massive clusters at a redshift of $z = 0.5$. In fact, these problems of weak-lensing mass determination, i.e., positive mass bias and large mass error dispersion, have been alluded in earlier works (Cen 1997; Reblinsky & Bartelmann 1999). Further, the cluster halo triaxiality itself can cause a bias in the lensing-based mass estimation (Clowe et al. 2004; Hamana et al. 2004; Oguri et al. 2005), while it is likely to have less effect on the X-ray cluster mass estimate (Gavazzi 2005). Thus, despite that weak lensing offers a unique tool for the measurement of cluster masses without any assumption of their equilibrium state, it can however suffer from the projection effects. Such problems are less significant in X-ray or spectroscopic velocity-dispersion measurements.

The present study aims to investigate the errors in weak lensing cluster mass measurements as well. However, this work differs from the aforementioned previous works, in that we attempt to simulate the actual wide-field weak lensing measurements, with numerically simulated shear data as closely resembling the observing data as possible. In particular, we shall focus on the bias errors and random errors pertinent to local weak-lensing measurement of ζ -statistic. Moreover, at a given observing depth, the finite number of background galaxies can introduce non-negligible Poisson noise convolved with the projection error in the measured data. We shall quantify, in this work, the regime for which the projection effect dominates, and the other regime where the Poisson noise dominates.

This paper is organized as follows. In Sect. 2 we describe our cosmological N -body simulations, weak lensing simulations, and the construction of a mock cluster catalog. Details of our shear-based mass estimator and mock observations are presented in Sect. 3. In Sect. 4 we apply the shear-based mass estimator to our simulated weak lensing observations, and examine the statistical properties of the errors in weak lensing cluster mass estimates. The radial mass error profiles are discussed in Sect. 5. Based on the radial error profiles, we propose a plausible alternative cluster mass indicator that has much reduced error dispersion. We finally present the discussions and a summary in Sect. 6.

2. Simulations

2.1. Particle N -Body Simulation and Weak Lensing Simulation

We use the Gadget code (Springel et al. 2001) to run 10 sets of independent simulations with 128^3 dark matter particles for a Λ CDM model in a $100h^{-1}$ Mpc cubic box. The cosmological parameters are $\Omega_m = 0.3$, $\Omega_\Lambda = 0.7$, the Hubble parameter $h = H_0/100\text{km/s/Mpc} = 0.7$, and the linear mass fluctuation amplitude $\sigma_8 = 0.94$. The mass resolution is $3.2 \times 10^{10} M_\odot$ per particle. We also conduct one simulation of 8 times higher mass resolution with the same initial condition for checking the convergence of the result.

General methods of backward ray-tracing have been detailed in Wambsganss et al. (1998) and Jain, Seljak, & White (2000). In the present study, on the other hand, we adopt a simpler linear approximation for the investigation of weak gravitational lensing. The shear matrices are generated on every lens plane with 4096^2 resolution, and we trace uniform 1024^2 rays backwards from the observer plane ($z = 0$) to the source plane ($z = z_S$). In the weak lensing approximation that employs the Born approximation, each photon travels along the un-perturbed trajectory, and the accumulated shear is the linear combination of gravitational shear given by every lens plane. Throughout this paper, we adopt a single source plane located at $z_S = 1$, which is the typical value for the mean redshift of background galaxies in an actual weak lensing survey with limiting magnitude $R \simeq 25.5$ mag (see Hamana et al. 2004). We then randomly choose a 1deg^2 field of view from the large projected simulation cubic box, and generate 36 lensing maps of 1deg^2 from each simulation. Ten sets of independent 100Mpc cosmological simulations were used to avoid the same clusters to be observed repetitively. Hence, the effective survey area is $36 \times 10 \times 1\text{deg}^2 = 360\text{deg}^2$.

To make sure the difference between 128^3 -particle simulation and 256^3 -particle simulation indeed negligible for cluster mass measurement, we compare 256^3 -particle simulation with 128^3 -particle simulation of the same initial condition for the weak lensing estimation of

cluster mass. It is found that two results are almost indistinguishable, for the following reason: The resolution of cluster mass estimation is limited by the finite galaxy number density, $n_g \sim 30$ galaxies per arcmin² which corresponds to the grid resolution of about 300×300 per deg². On the other hand, even a small cluster of $10^{14} M_\odot$ of redshift $z = 0.2$ contains 3000 particles within a projected area of 10 arcmin². The ten-times higher dark-matter particle number density than the background galaxy number density already warrants little clumpiness in mass distribution to arise from the discrete particle effect, thereby ensuring correct mass estimation even with lower resolution simulations.

2.2. Mock Cluster Catalog

We use the friends-of-friends algorithm (Huchra & Geller 1982) with linking-length 0.2 to search for clusters. After a cluster is identified, the center of mass position \mathbf{r}_c is then computed. We define the M_{200} of a cluster by increasing the enclosing spherical radius around the cluster center \mathbf{r}_c till it satisfies the criterion of r_{200} , within which the mean interior density is 200 times the mean density $\bar{\rho}(z) = \Omega_m(z)\rho_c(z)$ of the universe at the cluster redshift. Similarly, we define the cluster mass enclosed within r_{Δ_c} by

$$M_{\Delta_c} = \frac{4\pi}{3} \Delta_c \bar{\rho}(z) r_{\Delta_c}^3 \quad (1)$$

with Δ_c being the mean overdensity within r_{Δ_c} with respect to $\bar{\rho}(z)$.

In the end, we project the 3-D \mathbf{r}_c to obtain the projected cluster center, $\boldsymbol{\theta}_c$, and the projected r_{200} to θ_{200} , respectively. The peak position in the 2-D lensing map dose not necessarily coincide the center of mass position determined in 3-D particle simulation, especially in the case where the halo in 2-D projection contains substructures or mergers. From the observational viewpoint, the cluster center can be chosen from the local surface density peak. Nevertheless, we expect the difference not to be so serious as to affect the statistics of our mass estimate, since the difference between two centers is small compared with the inner most radius where the cluster mass estimate is made.

Through the above procedure, we obtain a mass-selected sample of about 4000 clusters with $M_{200} > 10^{14} M_\odot$ between lens redshifts $z = 0.2$ to 0.8 in our effective survey area 360deg^2 . Repeating clusters do occur in our randomly rendered maps but only at different cluster orientations and with different background and foreground lenses. For the purpose of the present work, which focuses on the measurement errors, repeating clusters can be regarded as independent samples since the noise is different.

3. Method

Our method for cluster mass estimation is based on the gravitational shear field, which is different from the method based on the convergence field used by Metzler et al. (2001) and White et al. (2002). Using the tangential component of galaxy shear for a lensing mass determination is often a preferred one, since it makes direct use of the locally observed galaxy ellipticities around the target cluster and is widely adopted in recent observations (Clowe et al. 2006; Bardeau et al. 2005; Jee et al. 2005). By contrast, the convergence-based method involves non-local mass reconstruction from the observation of galaxy ellipticities over a large field. Mathematically, the two methods are equivalent, and both exhibit the mass-sheet degeneracy. But in practice the local shear-field measurement has one additional degree of freedom in choosing an appropriate nearby control field as the background mass sheet to be subtracted.

3.1. Weak Lensing Formalism

We begin by briefly summarizing the basic formalism of weak gravitational lensing. A general review of weak lensing can be found in Bartelmann & Schneider (2001).

The deformation of an infinitesimal ray bundle due to gravitational deflection is described by a mapping between the two-dimensional source plane and the image plane as

$$\delta\beta_i = \mathcal{A}_{ij}(\boldsymbol{\theta})\delta\theta_j, \quad (2)$$

where $\boldsymbol{\beta}$ and $\boldsymbol{\theta}$ denote the angular position on the source and the image plane, respectively, and \mathcal{A}_{ij} is the 2×2 Jacobian matrix of the lens equation. In the weak lensing regime, the Jacobian matrix \mathcal{A}_{ij} is symmetric and can be decomposed as

$$\mathcal{A}_{ij} = (1 - \kappa)\delta_{ij} - \gamma_{ij}, \quad (3)$$

where γ_{ij} is the shear matrix defined as $\gamma_{ij} = \gamma_1\sigma_3 + \gamma_2\sigma_1$ with γ_i being the components of complex gravitational shear $\gamma := \gamma_1 + i\gamma_2$, σ_i being the 2×2 Pauli matrices, and κ being the lensing convergence responsible for the trace-part of the Jacobian matrix. The lensing convergence κ is a line-of-sight projection of the matter density contrast $\delta = (\rho_m - \bar{\rho})/\bar{\rho}$ out to the source plane (S) weighted by certain combination g of comoving angular-diameter distances (e.g., Jain et al. 2000),

$$\kappa = \frac{3H_0^2\Omega_m}{2c^2} \int_0^{\chi_S} d\chi g(\chi, \chi_S) \frac{\delta}{a} = \int d\Sigma_m \Sigma_{\text{crit}}^{-1}, \quad (4)$$

where a is the cosmic scale factor, and χ is the co-moving distance; Σ_m is the matter surface density $\Sigma_m = \int d\chi a(\rho_m - \bar{\rho})$ with respect to the cosmic mean density, and Σ_{crit} is the critical surface mass density of gravitational lensing,

$$\Sigma_{\text{crit}} = \frac{c^2}{4\pi G} \frac{D_S}{D_L D_{LS}} \quad (5)$$

with D_L , D_S , and D_{LS} being the angular-diameter distances from the observer to the lens, from the observer to the source, and from the lens to the source, respectively. The gravitational shear field is related with the lensing convergence field in a non-local manner (e.g., Bartelmann & Schneider 2001). The relation between κ and γ is expressed in Fourier space as (Kaiser & Squires 1993)

$$\hat{\gamma}_1(\mathbf{l}) = \frac{l_1^2 - l_2^2}{l_1^2 + l_2^2} \hat{\kappa}(\mathbf{l}), \quad (6)$$

$$\hat{\gamma}_2(\mathbf{l}) = \frac{2l_1 l_2}{l_1^2 + l_2^2} \hat{\kappa}(\mathbf{l}), \quad (7)$$

$$(8)$$

where $\hat{\kappa}(\mathbf{l})$ is the Fourier transform of $\kappa(\boldsymbol{\theta})$, $\hat{\gamma}_i(\mathbf{l})$ is the Fourier transform of $\hat{\gamma}_i(\boldsymbol{\theta})$, and \mathbf{l} is the Fourier variable conjugate to the angular position $\boldsymbol{\theta}$ on the sky. Equations (6) and (7) can be used to invert the gravitational shear field to the lensing convergence field.

3.2. The ζ - Statistic Mass Estimator

Jee et al. (2005) performed a weak lensing analysis on a $z = 0.8$ cluster, and found the mass estimate obtained from the aperture densitometry (Fahlman et al. 1994), or so-called the ζ -statistic, to be very close to that obtained from the nonlinear iteration-convolution method of Kaiser & Squires (1993). They also investigated the ζ -statistic within a projected aperture of $0.15r_{200}$, where the weak lensing assumption almost breaks down, and showed only about 10% mass error. Although the ζ -statistic can be accurate from the linear regime to the weakly nonlinear regime, this method however cannot avoid the projection effect arising from the foreground and background matter along the line-of-sight. In what follows, the mass errors caused by projection as well as other error sources will be quantified.

The observed image distortion of background galaxies can be directly used to derive the projected gravitational mass of clusters. The aperture mass estimate within the angular radius θ_1 , $M_\zeta(< \theta_1)$, in terms of the tangential component γ_T of gravitational shear can be expressed as

$$M_\zeta(< \theta_1) = \pi(\theta_1 D_L)^2 \Sigma_{\text{crit}} \zeta(\theta_1), \quad (9)$$

using the ζ -statistic defined as

$$\zeta(\theta_1) := \frac{2}{1 - \theta_1^2/\theta_2^2} \int_{\theta_1}^{\theta_2} d \ln \theta \langle \gamma_T(\theta) \rangle = \bar{\kappa}(< \theta_1) - \bar{\kappa}(\theta_1, \theta_2), \quad (10)$$

where $\langle \dots \rangle$ denotes the azimuthal average, and $\bar{\kappa} \equiv \bar{\Sigma}_m / \Sigma_{\text{crit}}$ is the mean convergence. Equations (9) and (10) show that the cluster mass can be measured from the galaxies ellipticity within the annulus bounded by θ_1 and θ_2 located just outside the mass to be measured.

As revealed in Eq. (10), the ζ -statistic yields the mean convergence interior to θ_1 , subtracted by the mean background within the annulus between θ_1 and θ_2 , $\bar{\kappa}(< \theta_1) - \bar{\kappa}(\theta_1, \theta_2)$. Hence, as long as $\bar{\kappa}(\theta_1, \theta_2) \ll \bar{\kappa}(< \theta_1)$, the enclosed mass within θ_1 can be obtained by multiplying ζ by the area $\pi \Sigma_{\text{crit}} (D_L \theta_1)^2$. As the inner radius θ_1 can almost be arbitrarily chosen to obtain the aperture mass within θ_1 , when θ_1 is chosen to be θ_{200} , the aperture mass M_ζ is approximately the cluster mass, M_{200} . Obviously, the aperture mass is smaller than the enclosed mass by a negative compensating mass that serves to remove the contribution from a background uniform mass sheet, and the degree of deviation depends on how steep the density profile is. In §4.3, we will demonstrate empirically that the negative compensating mass can actually correct for the systematic positive bias resulting from the projection effect.

The ζ -statistic is a spherically symmetric mass estimator. It gives rise to some errors for the typically irregular cluster. Nevertheless, this effect has been estimated less than 10% (Clowe et al. 2004). To avoid this effect to influence our cluster mass estimation, the number of clusters in the sample is crucial. Our sample of 4000 clusters contains clusters of different sizes and shapes, and the effect of non-spherical lens is expected to average out. Moreover, to avoid strong lensing, our mass estimator avoids the shear measurement near the cluster center (see §4.4).

The choice of the parameter θ_2 may also affect the cluster mass estimate. For example, a small θ_2 will generate large Poisson noise since the galaxy number for shear estimate within the annulus bound by θ_1 and θ_2 is not sufficiently large. On the other hand, if θ_2 is too large, the cluster mass measurement can be contaminated by the neighboring clusters in a crowded field. In practice, we nevertheless obtain similar results for $\alpha \equiv \theta_2/\theta_1 = 1.15, 1.2, 1.3$ and 1.4 with $\theta_1 = \theta_{200}$. Bardeau et al. (2005) and Jee et al. (2005) adopted the parameter α of 1.22 and 1.15 , respectively. Throughout this paper, unless otherwise noted, we use $\alpha = 1.2$ for the measurements of M_{200} .

For a projected lens system, $\langle \gamma_T \rangle$ is produced not only by the cluster itself but also by the projected neighboring clusters and large scale structures. As extreme examples, Figs. 1 and 2 show two convergence maps that give rise to large errors in the cluster mass estimate.

Figure 1 shows a simulated cluster of underestimated M_{200} , since a high mass cluster of

different redshift is located just in the annulus bounded by θ_1 and θ_2 . The underestimated mass can become negative. Figure 2 shows a cluster of overestimated M_{200} , as another cluster of different redshift is enclosed by θ_1 . In this case the cluster mass is overestimated by a factor >2 . Both Figs. 1 and 2 have fields of view of $1.2\theta_{200}$ defined by the central objects. Peculiar clusters of this kind are included in our raw sample of 4000 clusters.

3.3. Adding Noise

Another important factor that strongly influences the mass measurement is the galaxy intrinsic ellipticity, which plays a role as random noise in the shear measurement. In the weak lensing regime, the shear induced by gravitational lensing is some slight distortion of galaxy images, e.g., 10% distortion for cluster lenses. However, individual galaxies have an intrinsic ellipticity of random orientation with considerable dispersion, about 30–40%. Such orientation noise can only be reduced by taking average over some sufficiently large projected area around the lens.

In our simulation, the two components of the complex galaxy intrinsic ellipticity, $\epsilon_\alpha^{\text{int}}$ ($\alpha = 1, 2$), are generated by Gaussian random numbers with dispersion $\sigma_\gamma/\sqrt{2}$ per component. In the weak lensing approximation where $\kappa \ll 1$ and $|\gamma| \ll 1$, the net ellipticity $\epsilon_\alpha^{\text{net}}$ is a linear combination of galaxy intrinsic ellipticity $\epsilon_\alpha^{\text{int}}$ and gravitational shear γ_α , that is,

$$\epsilon_\alpha^{\text{net}} = \epsilon_\alpha^{\text{int}} + \gamma_\alpha. \quad (11)$$

In what follows, we assume a weak lensing survey of mean galaxy surface number density, $n_g = 30 \text{ arcmin}^{-2}$, and intrinsic ellipticity dispersion, $\sigma_\gamma = 0.4$, in our simulations.

3.4. Mass and Redshift Bins of Cluster Sample

Given a finite number of sample clusters in the simulation, we focus on those clusters that can produce sufficiently strong signals for the weak-lensing mass determination. This issue is important in the context of this study, as we are interested in the observational uncertainties in the cluster mass determination. Clusters of unsuitable mass and redshift ranges will yield unreasonably high uncertainties to provide useful astrophysics information. Our sample of clusters is selected based on the mass (e.g., White et al. 2002), whereas practical weak lensing samples of clusters are “shear-selected”, that is, weighted by both the mass and the redshift (e.g., Reblinsky & Bartelmann 1999; Hamana et al. 2004). A concise overview of how clusters of viable mass redshift ranges are determined is given below. It

provides a criterion for us to select those "clean" clusters from 4000 clusters in the raw sample.

Typical cluster search schemes use the convergence map instead of the shear map (e.g., White et al. 2002; Padmanabhan et al. 2003; Hamana et al. 2004). In this method one first adopts a Gaussian filter to smooth the raw convergence κ map, followed by identification of local peaks in the smoothed convergence map with a certain threshold. The threshold signal-to-noise ratio (S/N) in the smoothed κ -map is given as $\nu = \kappa_G/\sigma_\kappa$ with rms noise in the κ_G -map, $\sigma_\kappa = \sigma_\gamma/(4\pi\theta_G^2 n_g)^{1/2}$ with the Gaussian smoothing scale $\theta_G \equiv \text{FWHM}/\sqrt{4\ln(2)} \simeq 0.02(\sigma_\gamma/0.4)(n_g/30\text{arcmin}^{-2})^{-1/2}(\theta_G/1')^{-1}$.

An optimal choice for the threshold ν depends on the concentration parameter of the NFW profile, c_{NFW} , the cluster mass M_{cl} and the lens redshift z_L . Moreover, the optimal threshold ν can be quantified in terms of the survey completeness and efficiency. For a weak lensing survey with $n_g = 30 \text{ arcmin}^{-2}$ and $z_S = 1$, corresponding to an actual survey with limiting magnitude $R \simeq 25.5$ mag under a subarcsec seeing condition, Hamana et al. (2004) found that the threshold $\nu \sim 4$ with $\theta_G \sim 1'$ provides an optimal balance between survey completeness and efficiency. At the optimal threshold $\nu \sim 4$, the lower mass detection limits are then $M_{\text{cl}} = 10^{14}M_\odot$, $2 \times 10^{14}M_\odot$, and $4 \times 10^{14}M_\odot$ for lens redshift ranges of $0.2 < z_L < 0.4$, $0.2 < z_L < 0.6$, and $0.2 < z_L < 0.8$, respectively. We therefore divide the cluster mass into three mass bins:

$$10^{14}M_\odot < M_1 < 2 \times 10^{14}M_\odot, \quad (12)$$

$$2 \times 10^{14}M_\odot < M_2 < 4 \times 10^{14}M_\odot, \quad (13)$$

$$M_3 > 4 \times 10^{14}M_\odot, \quad (14)$$

where M_1 , M_2 , and M_3 are defined with the M_{200} . The above three redshift bins are also adopted in this study. The cluster numbers in different mass bins and different redshift intervals in our sample are given in Table 1.

4. Mass Probability Distribution Function

For each cluster in our mock cluster sample, we determine the cluster mass M_{true} using the N -body simulation data and the lensing mass $M_{\text{lens}} = M_\zeta$ using the ζ -statistic (10). We note that both M_{true} and M_{lens} are projected masses enclosed by a cylinder of certain radius $D_L\theta$ which is relevant to gravitational lensing. For the true mass M_{true} , the integral along the line-of-sight is taken only within r_{200} from the cluster center, while it is taken over the line-of-sight from $z = 0$ to $z = z_S$. When the angular radius θ is taken to be $\theta_{200} \equiv r_{200}/D_L$, then $M(< \theta_{200}) \approx M_{200}$. Collecting all clusters of $M_{200} > 10^{14}M_\odot$ from the simulation data,

we then construct the observed mass probability function $P(\mu)$ with

$$\mu(\theta) \equiv \frac{M_{\text{lens}}(< \theta)}{M_{\text{true}}(< \theta)}. \quad (15)$$

However, as will be elucidated later, a substantial fraction of lenses are suffered from the projection effect as well as strong observational noise due to intrinsic galaxy ellipticities, both of which yield considerable errors in the mass measurement. To reduce such errors in the mass determination, we conduct a simple-minded "clean sample" procedure, which removes those clusters from our raw sample that obviously contain nearby objects in the convergence map, and/or those clusters whose mass is below a redshift-dependent limiting mass (§4.2).

We nevertheless note that even in the clean sample, mass estimates from the ζ -statistic still contain residual mass errors due to local filamentary structures around the target cluster as well as intervening large-scale fluctuations (i.e., cosmic shear) projected along the line-of-sight, as shown in Fig. 3. The details of the clean procedure will be presented in Sec. 4.2. The numbers of clean clusters in three mass bins and three redshift intervals are listed in Table 2. Most of the removed samples contain contaminant objects of different redshifts due to chance projections along the line-of-sight. Only a small fraction contain physically nearby objects and mergers, and the parenthesis in Table 2 gives the percentage of removed samples that belong to this category.

4.1. Raw Sample

The observational errors of M_{200} is examined from our raw sample. The result derived from the raw sample serves as a baseline for comparison with those derived from the clean sample. The mass probability distribution function is defined as $P(\mu) \equiv dn/(N_z d\mu)$, where N_z is the total cluster number in a given redshift bin, $d\mu$ the mass error bin, and dn the cluster number in the mass error bin at a given redshift.

Two cases are separately investigated: the noise-free case that yields Fig. 4, and the noisy case that yields Fig. 5. The noise-free case contains measurement errors due solely to the projection effect, and the mass probability function is positively skewed with a tail. Nevertheless, we find the peak at $\mu \approx 1$, which is in agreement with White et al. (2002).

On the other hand, the noisy case contains contaminations from both projection and galaxy ellipticity effects. The random Gaussian noise due to intrinsic galaxy ellipticities adds substantial errors to the gravitational shear estimate, giving rise to a mass probability function considerably more symmetric and broader than the noise-free case.

The error bars in both Figs. 4 and 5 represent the intervals of 68% confidence. We note that for the noisy case, the confidence intervals are obtained by averaging over 20 independent galaxy realizations. Due to the Gaussian nature of the galaxy ellipticity noise, the S/N can be improved in a predictable manner as $\sqrt{N_g}$, where N_g is the number of background galaxies used to determine the cluster mass. Hence, high-redshift clusters, being smaller in angular size, have noisier mass estimates than low redshift clusters. Furthermore, as high-redshift clusters are not optimally located for the $z_s = 1$ source galaxies, only massive ones can yield reasonably acceptable mass determination.

The mass-error dispersion of the respective mass probability functions in three different redshift intervals is given in Table 3. It is clear that the error dispersion for the raw sample is so large that the mass measurement can hardly be in good use for construction of the mass function. Again, Table 3 serves as the baseline for comparison against the error dispersion resulting from the clean sample.

4.2. Clean Sample

We apply a "clean" procedure to the raw cluster sample (§4.1) in order to remove clusters that would yield unreliable mass estimates from the ζ -statistic mass estimator (§3.1). Our clean procedure consists of the following two steps: The first step is to remove clusters whose masses are below a weak-lensing detection limit. Adopting the result of Hamana et al. (2004), we first set lower limiting masses of $M_{200} = 4 \times 10^{14} M_\odot$, $2 \times 10^{14} M_\odot$, and $10^{14} M_\odot$, for clusters in redshift ranges of $0.2 < z < 0.8$, $0.2 < z < 0.6$, and $0.2 < z < 0.4$, respectively (see §3.3). The clean sample contains only these clusters selected by the redshift-dependent limiting masses $M_{200}(z_L)$ above. The sample after this first cleaning procedure can be regarded as an effective "shear-selected" sample of clusters. The second step is to remove those clusters which have detectable "nearby" clusters in the projected map located within $1.2\theta_{200}$ from the target cluster. After the above removal procedure the remaining randomly rendered maps contain only the clean clusters that constitute our clean sample. Table 2 shows the cluster numbers of the clean sample in different mass and redshift bins, as well as the percentage of removed clusters that have genuinely nearby contaminants in the physical space.

The clean procedure reduces the projection effect in the shear-based cluster mass estimate, and the benefit of "clean" is found to be only moderate as revealed by the error dispersions of the clean sample in Table 4. A comparison between Tables 3 and 4 shows that the clean sample has 15% improvement for the least massive clusters of low-redshift to 50% for the most massive clusters of high-redshift in the noise-free error dispersion. When observational noise due to intrinsic galaxy ellipticities is included, the clean sample is at

most 30% better in error dispersion. Such a result cannot be considered to be satisfactory. Clearly, there is still much room for improvement in error reduction. This will be the subject of §4.4 and 4.5.

4.3. Moments of Clean-Sample Mass Probability Distribution Functions

Figure 6 depicts the mass probability distribution functions $P(\mu_{200})$ of $\mu_{200} \equiv M_{\text{true}}(< \theta_{200})/M_{\text{lens}}(< \theta_{200})$ in noisy and noise-free simulations for different mass-bins and redshift-intervals derived from the clean sample. The statistical properties of a probability function can be characterized by its distribution moments, such as the mean, the dispersion, the skewness, and other higher-order moments. We compute these first three moments to quantify the mass probability function for the 3 mass bins and 3 redshift intervals. The results are listed in Tables 4, 5 and 6.

The mass probability function tends to have a positive tail and be asymmetric. The positive offset can be characterized by the skewness S_3 tabulated in Table 6. The skewness is defined to be the third moment of the distribution function: $S_3 := \sum_{i=1}^N (\mu_i - \bar{\mu})^3 / ((N - 1)\sigma^3)$. This parameter is a measure of non-Gaussianity originated from the projection effect, since the contaminant lenses are non-Gaussian. However, inclusion of the galaxy ellipticity noise substantially reduces the skewness, thus making the mass probability function more symmetrical about the peak.

Note from Table 5 that the mean is found to be only slightly greater than the peak (≈ 1) shown in Fig. 6 as a result of the small positive skewness of the distribution. To be specific, the mean has a positive bias of less than 10% for clusters of all mass and redshift ranges in our clean sample. Moreover, the positive bias increases only slightly with increasing lens redshift. The fact that the ζ -statistic mass estimator has a small bias is surprising, since it is at variance with a previous study. White et al. (2002) adopted to use the convergence map for a weak-lensing mass measurement, and showed a 20% positive mass bias for massive clusters of intermediate redshifts. Such a positive bias results from the projection effect by local large-scale structures surrounding the target galaxy cluster that accounts for an additional 20%–30% lensing strength (Metzler et al. 1999; Metzler et al. 2001).

In contrast to the κ -based mass measurement, the local shear-based mass measurement with ζ -statistic turns out to have a compensating effect to neutralize the anticipated positive bias. Weak lensing measurements are subject to the mass-sheet degeneracy (Bradac et al. 2004), which renders the uniform background matter undetectable. In the κ -based mass measurement, the overall field tends to be so large as to permit an accurate global inversion

of the convergence field. The background so defined is therefore the global background over a large field. On the other hand, the shear-based measurement is a local measurement and the background matter density is defined only locally in the projection space. The second term in Eq. (10) is exactly the local background surface density defined over a control field within an annulus just outside the target field. Hence while the environment surrounding the cluster is rich in matter, the matter density in the control field just outside the aperture of the target field can be correspondingly high as to cancel the enhanced background contribution along the line-of-sight of the target field. The cancellation significantly reduces the positive bias of the lensing mass.

To show the cancellation of the bias, we compute the ratio of the noise-free local mass $\Delta M(\theta_1, \theta_2) = \pi \Sigma_{\text{crit}} D_L^2(\theta_2^2 - \theta_1^2) \bar{\kappa}(\theta_1, \theta_2)$, contained in the second term in Eq. (10), to the true cluster mass M_{true} , where all matter outside $50h^{-1}\text{Mpc}$ from the target cluster has been excluded for examination of the local contribution to the projection effect. Here we take $\theta_1 = \theta_{200}$ and $\theta_2 = 1.2\theta_1$. Table 7 shows the means and the variances of this ratio for all clusters in the clean sample. The mean ratio ranges from 18% to 26% with a considerably small variance.

Indeed, the mean ratio has a correct value to largely cancel the well-known mass over-estimation of 20 – 30% produced by the local projection effect (Metzler et al. 1999; Metzler et al. 2001; White et al. 2002). This result quantitatively demonstrates the self-cancellation of two environmental contributions to be at work with ζ -statistic. The possibility of such a cancellation was previously alluded by Metzler et al (1999), but the small number of sample clusters prevented them from drawing a quantitative conclusion.

Coming back to Table 4, we find the error dispersion for the noise-free case tends to be small at redshift intervals in between $0.4 < z_L < 0.6$. This is because the source galaxy redshift $z_S = 1$ favors lensing signals from this lens redshift. The noise-free result for the high mass bin, M_3 , at $0.4 < z_L < 0.6$ can be compared with the result of Metzler et al. (2001) for $z = 0.5$. They obtained an error dispersion $\sigma = 0.26$ in the ratio between the estimated M_{200} and the true M_{200} , which is in good agreement with the noise-free error dispersion in our clean sample, $\sigma = 0.28$. On the other hand, for the noisy case, the smallest error dispersion occurs at lens redshift interval $0.2 < z_L < 0.4$. It means that the errors contributed by galaxy ellipticity noise is significant, and the larger angular size of low- z lens, having a larger sampling annulus, helps reduce the sampling noise. Table 4 also shows that the cluster mass measurement errors can be significantly enhanced by the galaxy ellipticity noise by more than almost 50% for all lenses, except for the highest mass and lowest redshift bin. This indicates that the dominant error source in the weak lensing M_{200} can be the galaxy ellipticity. This finding motivates us to proceed on seeking an alternative mass estimator

below.

4.4. Radial Mass Error Profile

We turn to the radial profile $\mu(\theta) = M_{\text{lens}}(< \theta)/M_{\text{true}}(< \theta)$, measured for individual clusters of the clean sample. We fix the outer radius θ_2 to be $1.2\theta_{200}$ and vary the mass-aperture radius θ_1 . The results are presented in Fig. 7 for the noise-free and noisy cases. The innermost radius is chosen to be $0.2\theta_{200}$ so as to stay in the observationally weak-lensing regime. For a typical cluster in our clean sample, $r_{200} \approx 1h^{-1}\text{Mpc}$ and the innermost radius limit is about $200h^{-1}\text{kpc}$, which is mostly outside the scaling radius of the NFW profile.

The error bars in Fig. 7 represent 68% confidence levels around the estimated mean $\mu(\theta)$, obtained over 20 independent background realizations similar to Fig. 5. The deviation of the mean- μ from unity indicates a systematic bias. Very little systematic bias is detected interior to θ_{200} in Fig. 7.

The error bars in Fig. 7 are seen to decrease with decreasing radius. In particular, the mass error caused by intrinsic galaxy ellipticities (i.e., the difference between error bars of noisy and noise-free cases) decreases mostly noticeably for $\theta_{200} > \theta > 0.7\theta_{200}$. This feature arises from the peculiar feature of ζ -statistic, where the enclosed mass within a smaller radius is measured by a larger annulus. Such an error stays relatively constant for $\theta \lesssim 0.7\theta_{200}$, which can be understood from the geometry. The annulus area enhancement begins to saturate when the inner radius becomes smaller than half the outer radius. On the other hand, the projection errors continue to decrease at the ever decreasing radius. This trend can be understood from the second equality of Eq. (10). For a small θ_1 , the interior convergence $\bar{\kappa}(\theta_1)$ is much greater than the average convergence in the annulus $\bar{\kappa}(\theta_1, \theta_2)$, which contains lensing contributions of other redshifts. It therefore becomes increasingly insensitive to most contaminant lenses for a decreasing θ_1 .

4.5. Alternative Weak-Lensing Mass Estimators?

Section 4.3 already reveals the considerably large errors arising from galaxy ellipticity in the weak lensing mass measurements. On the other hand, Sec. 4.4 also shows that despite a sizable error in the measured M_{200} , the error becomes substantially small for the fractional mass well within r_{200} . This tendency has also been noticed by Metzler et al. (2001) and Cen (1997) previously for noise-free mass estimations.

In order for the weak-lensing measurement to yield a reliable cluster mass estimate,

we seek an alternative mass estimator that is contaminated by the ellipticity noise and the projection effect to a much lesser degree. In Table 8, we enlist the ever-decreasing mass errors for the 2D projected mass measured over the decreasing radii, θ_{500} , θ_{1000} , and θ_{1500} . Here $\theta_{\Delta_c} \equiv r_{\Delta_c}/D_L$ is the projected angular radius of the 3D interior mass M_{Δ_c} defined by Eq. (1). These radii correspond, on average, to $\theta = 0.7\theta_{200}$, $0.5\theta_{200}$, and $0.4\theta_{200}$, respectively, in weak dependence on the lens mass and redshift. Projected masses evaluated at these radii contain significantly smaller errors than M_{200} , and may serve as alternative mass indicators.

A similar proposal was put forth for the mass estimator of X-ray clusters. With cosmological simulations, Evrard et al. (1996) found that X-ray mass estimates are remarkably accurate when evaluated at radii from r_{500} to r_{2500} . Recent X-ray observations measure the cluster mass at r_{500} (Finoguenov et al. 2002) and at r_{2500} (Allen et al. 2002). Moreover, Jee et al. (2005a) compared the cluster mass profiles derived from X-ray and from weak lensing, and found increasing agreement with decreasing radii. The radius r_{2500} is about $0.3r_{200}$ for our sample clusters. In fact, the mass within $0.3\theta_{200}$ may be accurately measured by weak lensing even at a lens redshift of $z_L \sim 0.8$, as discussed by Jee et al. (2005b). However, the cluster mass within $0.3r_{200}$ can be sensitive to the complex interior structures of a cluster, for example, containing two cores in a cluster recently undergoing a merger, and/or the baryonic physical processes such as radiative cooling and galaxy formation. Moreover, for a dual-core cluster, r_{2500} can be ambiguous to define.

We therefore suggest that $M(< \theta_{1000})$ be a better weak-lensing mass estimator. On one hand, it has an acceptable worst mass errors ($< 39\%$) for the 3 mass bins and different redshift intervals, as revealed in Table 8. On the other hand, the radius is still sufficiently large, $\sim 0.5\theta_{200}$, so that the mass estimator can be insensitive to the cluster interior structures. Finally, $M(< \theta_{1000})$ is a significant fraction of M_{200} and it should still follow the well-known similarity scaling of the CDM gravitational collapse.

5. CONCLUSIONS

This paper reports a systematic study on the accuracy of cluster mass measurements through weak lensing observations. Specifically this work takes into account the mass errors introduced by the projection effect and by the Poisson noise of finite number of randomly oriented background galaxies. Among these sources of mass errors, the projection effect has been reported to yield a non-negligible systematic positive bias ($\sim 20\%$) in the cluster mass estimate based on weak lensing. Adopting the local shear-field measurement using ζ -statistic, which is often used in actual observations, we nevertheless found that such a positive bias can be largely canceled by the positively-biased local background mass sheet.

That is, the ζ -statistic measurement can provide a bias-free cluster mass estimate.

In this paper, we also report that the error in M_{200} determination is expected to exceed 50% even for a moderately deep observation ($R \simeq 25.5$ mag), regardless of lens mass and redshift. Even after a clean procedure that removes clusters with detectable companions in the projected map, the mass error is still substantial, exceeding 40% for a $R \simeq 25.5$ observation. Mass errors can scatter observed data of one mass bin into another bin when constructing the cluster mass function, and smear out the mass function. In the mass range where the mass function has a large gradient, i.e., $M > M_*$, such mass errors can greatly distort the mass function. The measurement error will eventually propagate into the determination of cosmological parameters, such as the matter density parameter Ω_m and the matter fluctuation amplitude σ_8 , which rely critically on an accurate mass function. The so-called self-calibration was devised to correct for the systematic errors of this kind (Hu 2003), but the random errors are un-removable even with the self-calibration.

To significantly reduce the mass error in weak lensing measurements, we also suggest the possibility of an alternative lens mass, which has a considerably smaller error. It is an interior mass well inside θ_{200} . For example, Fig. 7 shows that the error in $M(< \theta_{500})$ (mass interior to approximately $0.7\theta_{200}$) is already noticeably smaller than M_{200} , the error dispersion of $M(< \theta_{1000})$ is at most 39% for all detectable clusters and the error dispersion of $M(< \theta_{1500})$ at most 32%. Comparing Table 8 with Table 4, we find M_{1000} to have more than a factor 2 in error reduction for all detectable clusters; for low- z lenses, the error reduction can be as large as a factor 3. Given these results, we suggest that $M(< \theta_{1000})$ be a better mass variable than M_{200} for constructing the mass function.

Concerning the mass function of $M(< \theta_{1000})$, it should be reminded that the mass function of M_{200} cannot be analytically derived, and needs to be determined empirically from N -body simulations. From this spirit, the mass function of $M(< \theta_{1000})$ can also be obtained from N -body simulations, in a similar manner as the mass function of M_{200} . To the best of our knowledge, there have not been investigations on the mass function for mass different from M_{200} in literature. Such a new class of mass function, containing less mass scatter than the conventional mass function, may be more useful for constraining the cosmological parameters. However, whether or not the more accurately measured $M(< \theta_{1000})$ function can actually be more useful than the less accurately measured M_{200} function really depends on the detailed form of the $M(< \theta_{1000})$ function that contains the cosmology-parameter-sensitive feature, similar to a break at M_* for the M_{200} function. Therefore our suggestion at this point in favor of an alternative mass estimator for a new mass function should be regarded as plausible but still preliminary.

Finally, though the depth of observation has been fixed to $R \simeq 25.5$ mag in this work for

which $n_g \simeq 30 \text{ arcmin}^{-2}$, for evaluation of mass errors, we may relax this constraint to assess other observing depths straightforwardly. At a medium depth $R \simeq 24.5 \text{ mag}$, suitable for wide-field surveys, the background galaxy density $n_g \simeq 20 \text{ arcmin}^{-2}$ (Fontana et al. 2000). One can quickly estimate from Fig. 7 with the Poisson statistics that the galaxy ellipticity noise is still much less than the errors at θ_{500} , θ_{1000} , and θ_{1500} introduced by the projection effect for clusters of $M > 2 \times 10^{14} M_\odot$ and $0.2 < z_L < 0.4$ and clusters of $M > 4 \times 10^{14} M_\odot$ and $0.2 < z_L < 0.6$. That is, a medium-depth observation can provide as an accurate mass measurement as a deep observation for those more massive and lower redshift clusters. Such information is crucial for the planning of wide-field surveys.

Acknowledgments

The authors would like to thank Masahiro Takada for useful discussions. This work is supported in part by the grant, NSC-94-2112-M-002-026, from National Science Council of Taiwan

REFERENCES

Allen, S.W., Schmidt, R.W., & Fabian, A.C. 2002, MNRAS, 334, L11

Bardeau, S. et al. 2005, A&A, 434, 433B

Bartelmann, M., & Schneider, P. 2001, Phys. Rep., 340, 4-5, 291

Bartelmann M. 1995 A&A, 303, 643

Bradac, M., Lombardi, M., & Schneider, P. 2004, A&A, 424, 13

Broadhurst, T., Takada, M., Umetsu, K., Kong, X., Arimoto, N., Chiba, M., & Futamase, T., ApJ, 619, 143L

Cen, R. 1997, ApJ, 485, 39

Clowe, D., De Lucia, G., & King, L. 2004, MNRAS, 350, 1038

Clowe, D. et al. 2006, A&A, 451, 395

Dahle, H., Pedersen, K., Lilje, P. B., Maddox, S. J., Kaiser, N., ApJ, 591, 662

Erben, T., van Waerbeke, L., Mellier, Y. et al. 2000, A&A, 355, 23

Erroti S. & Lombardi M 2003,

Evrard, A.E., Metzler, C.A., & Navarro, J.F. 1996, ApJ, 469, 494E

Fahlman, G., Kaiser, N., & Woods, D. 1994, ApJ, 437, 56

Finoguenov, A., Reiprich, T. H., & Böringer, H. 2001 ,A&A, 368, 749

Gavazzi, R. 2005, A&A, 443..793

Hamana, T., Takada, M., & Yoshida, N. 2004, MNRAS, 350, 893

Hennawi, J.F., & Spergel, D.N., 2005, ApJ, 624, 59

Hu, W., 2003, Phys. Rev., D67, 081304

Huchra, J. P., & Geller, M. J. 1982, ApJ, 257, 423

Irgens, R.J., & Lilie, P.B. 2002, 597, 227

Jain, B., Seljak, U., & White, S. 2000, ApJ, 530, 547J

Jee, M.J. et al. 2005, ApJ, 634, 813J

Jee, M.J. et al. 2005, ApJ, 618, 48

Kaiser N. 1995, ApJL, 439, L1

Kaiser, N., & Squires, G. 1993, ApJ, 404, 441

King, L.J., Schneider, P., & Springel, V. 2001, A&A, 378, 748

Metzler, C.A., White, M., Norman, M. & Loken, C. 1999, Apj, 520, L9

Metzler, C.A., White, M., & Loken, C. 2001, Apj, 547, 550

Miyazaki, S., Hamana, T., Shimasaku, K. et al. 2002, ApJ, 580, 97

Oguri, M., Takada, M., Umetsu, K., & Broadhurst, T. 2005, ApJ, 632, 841

Reblinsky K., & Bartelmann M. 1999, A&A, 345, 1

Schirmer, M., Erben, T., Hetterscheidt, M., Schneider, P. 2006, submitted to A&A (astro-ph/0607022)

Schneider, P. 1996, MNRAS, 283, 387

Schneider, P. 2005, astro-ph/0509252

Seitz S., & Schneider P. 1996, A&A, 305, 383

Springel, V., Yoshida, N., & White, S.D.M. 2001, New Astronomy, 6, 79

Squires G., & Kaiser N. 1996, ApJ, 473, 65

Tyson, J.A., Wenk, R.A., & Valdes, F. 1990, ApJ, 349, L1

van Waerbeke, L. 2000, MNRAS, 313, 524

Umetsu, K., Tada, M., Futamase, T. 1999, Prog. Theor. Phys. Suppl., 133, 53

Umetsu, K., & Futamase, T. 2000, ApJ, 539, 5

Umetsu, K., Wu, J.M., Chiueh, T. & Birkinshaw, M. 2005, submitted to ApJ (astro-ph0506065)

Wambsganss, J., Bode, P., & Ostriker J. 2004, ApJ, 606, L93-L96

White, M., van Waerbeke, L., & Mackey, J. 2002, ApJ, 575, 640

Wittman, D, Margoniner, V. E., Tyson, J. A. et al. 2003, ApJ, 597, 218

Wittman, D, Tyson, J. A., Margoniner, V. E. et al. 2001, ApJ, 557, 89

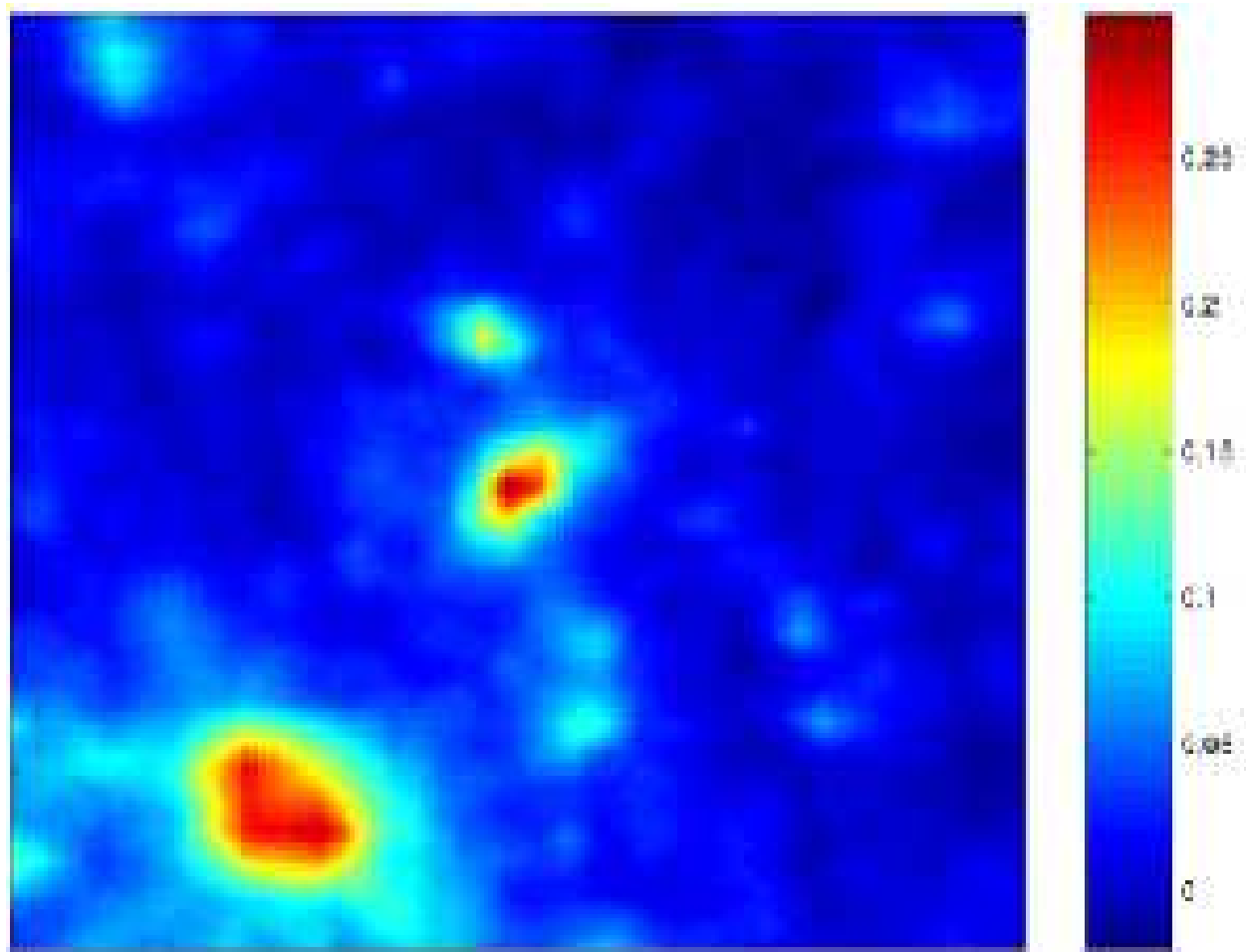


Fig. 1.— An example of the raw κ map that produces a negative M_{200} for the target cluster at the center, where the object on the lower-left corner is located at a different redshift. The field of view is $1.2\theta_{200} \times 1.2\theta_{200}$ defined by the central cluster.

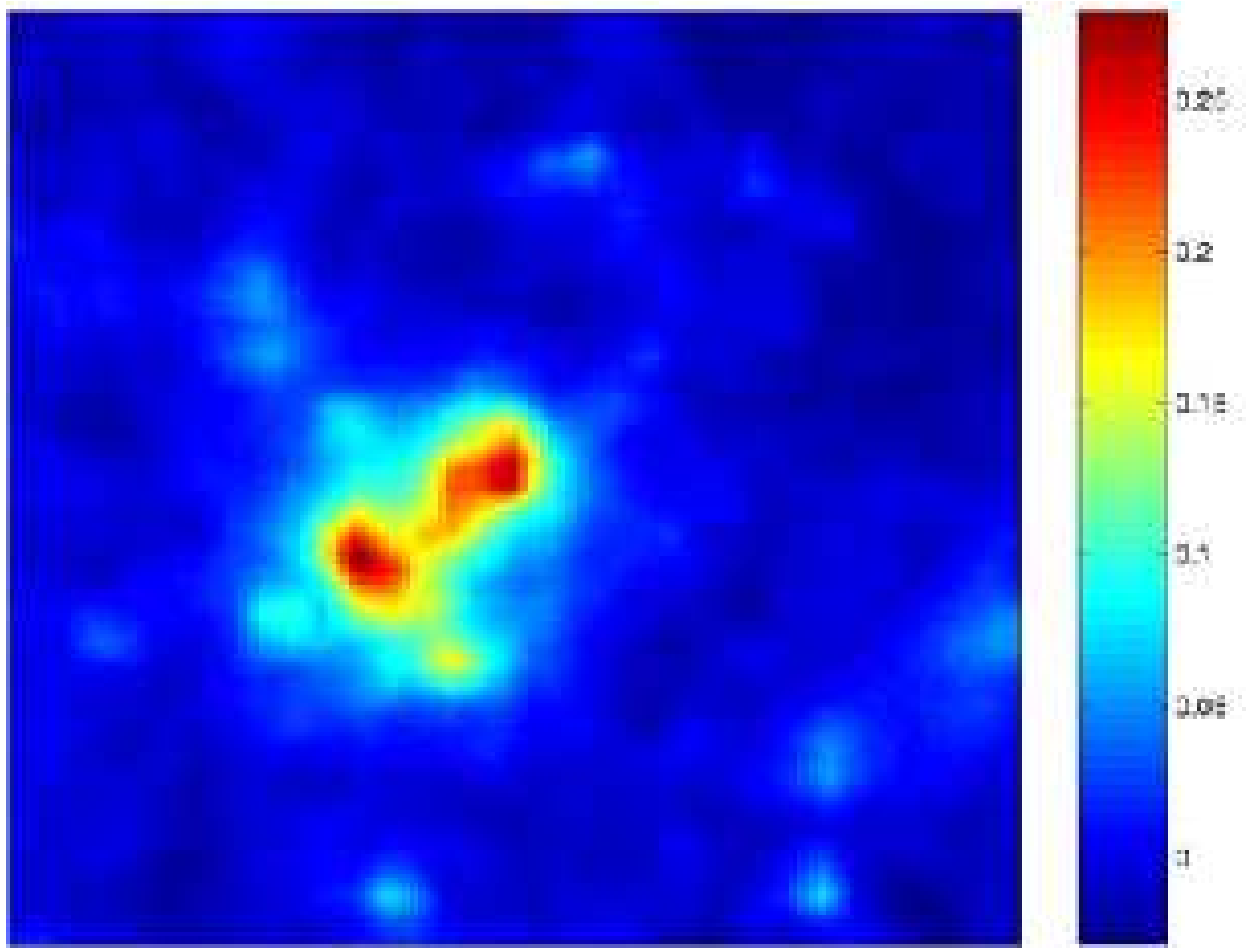


Fig. 2.— An example of the raw κ map that produces an over-estimated M_{200} , where the nearby object in the map is also located at a different redshift. The field of view is defined in the same manner as in Fig. 1.

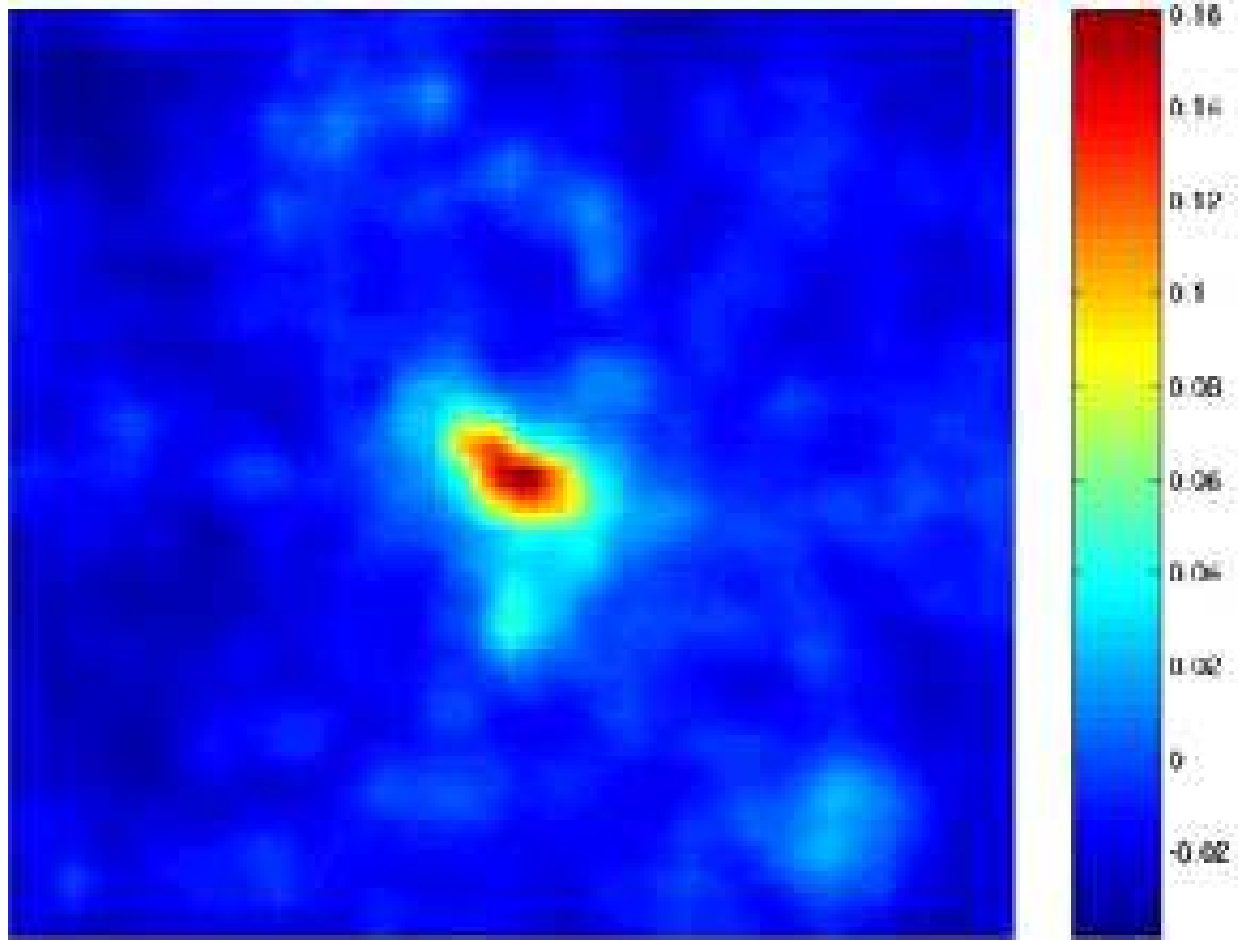


Fig. 3.— An example of clean κ maps, where contaminants have relatively low signal strengths.

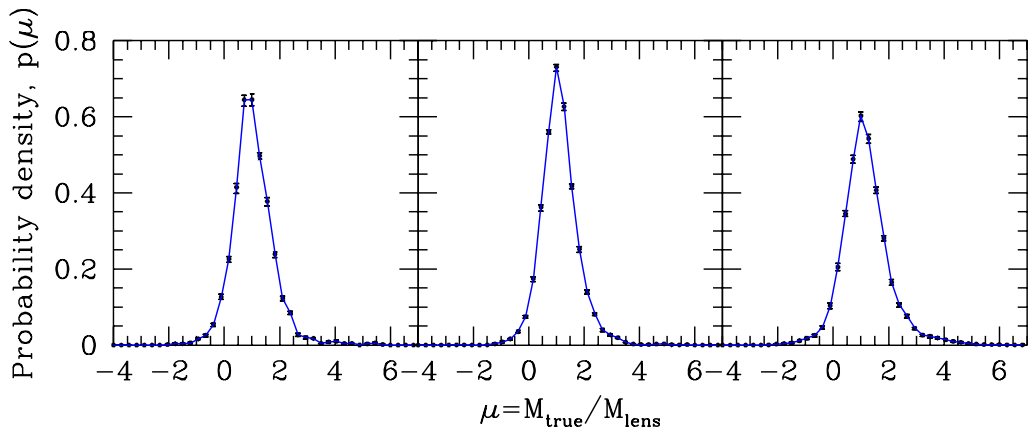


Fig. 4.— Mass probability distribution functions from noise-free simulations for three different redshift intervals as indicated in the figure. The error bars represent 68% confidence intervals from 20 independent galaxy realizations.

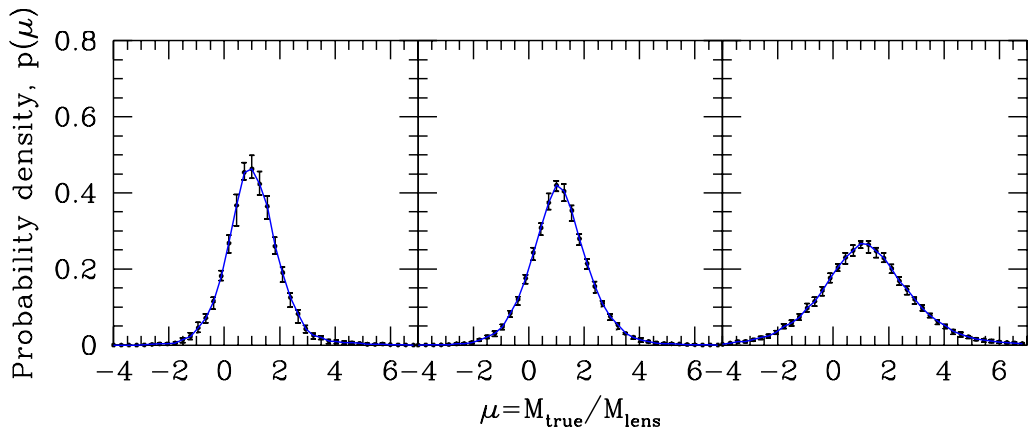


Fig. 5.— Mass probability distribution functions of noisy maps for three different redshift intervals as indicated in the figure. The error bars represent 68% confidence intervals from 20 independent galaxy realizations.

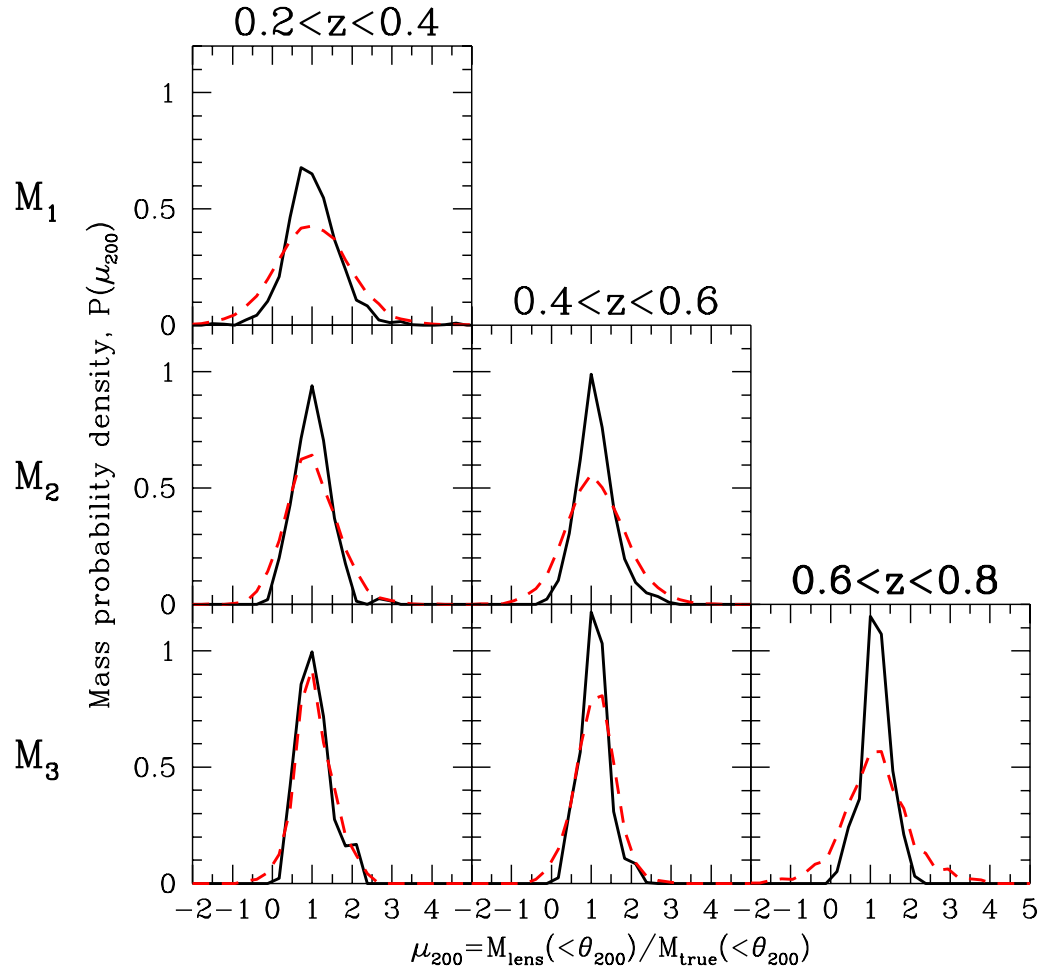


Fig. 6.— Noise-free (*solid*) and noisy (*dashed*) mass probability distribution functions of the clean sample for different bins of cluster mass and redshift: $1 < M_1/10^{14}M_\odot < 2$, $2 < M_2/10^{14}M_\odot < 4$, $M_3/10^{14}M_\odot > 4$. Here, the cluster mass refers to M_{200} .

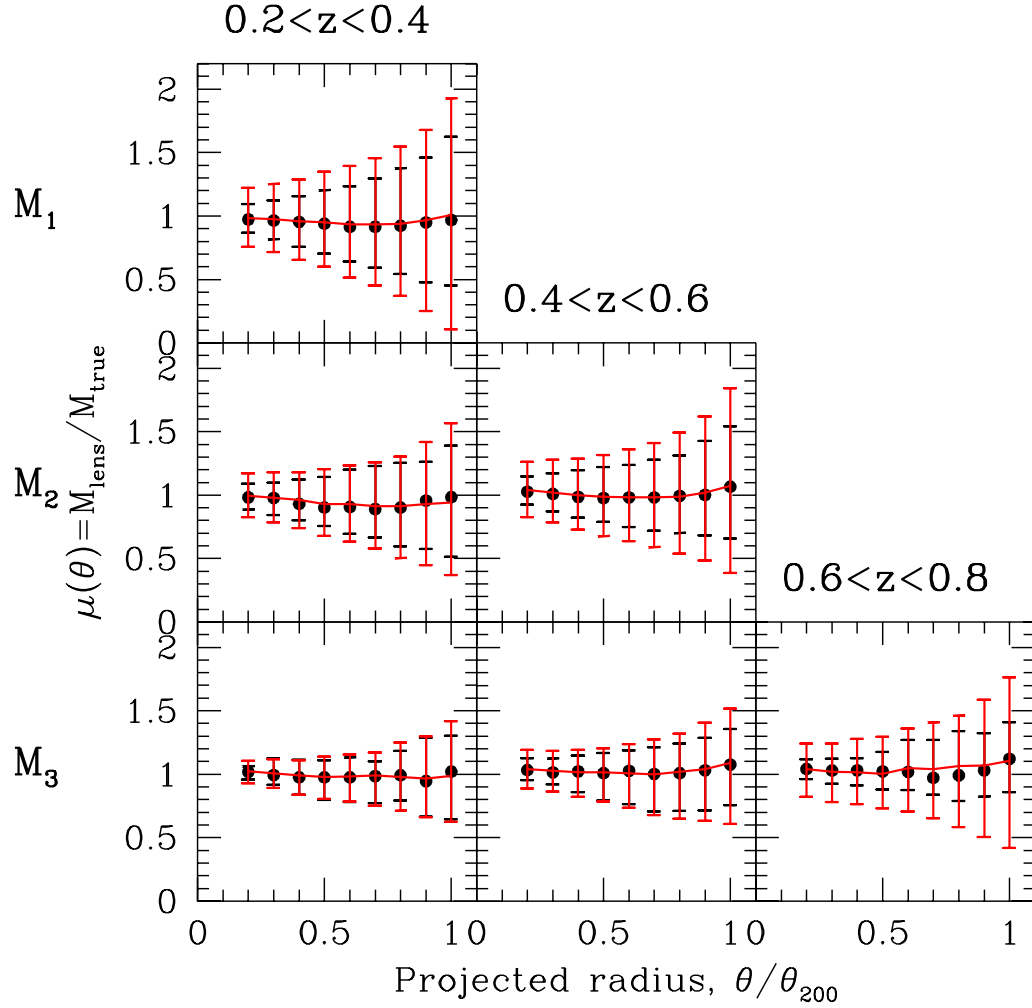


Fig. 7.— Noise-free (black) and noisy (red) projected-mass radial profiles of the clean cluster sample for different mass bins and redshift intervals: $1 < M_1/10^{14}M_\odot < 2$, $2 < M_2/10^{14}M_\odot < 4$, $M_3/10^{14}M_\odot > 4$. Mean values are represented by filled circles (black) for the noise-free case, and by connected lines (red) for the noisy case. The error bars indicate 68% confidence levels around the mean.

This preprint was prepared with the AAS L^AT_EX macros v5.0.

Table 1: Cluster number in the raw sample

	$0.2 < z < 0.4$	$0.4 < z < 0.6$	$0.6 < z < 0.8$
$1 < M_{200}/10^{14}M_{\odot} < 2$	444	1144	1374
$2 < M_{200}/10^{14}M_{\odot} < 4$	145	350	364
$M_{200}/10^{14}M_{\odot} > 4$	59	92	43

Table 2: Cluster number in the clean sample and percentage of interacting clusters among those that are removed during the clean

	$0.2 < z < 0.4$	$0.4 < z < 0.6$	$0.6 < z < 0.8$
$1 < M_{200}/10^{14}M_{\odot} < 2$	324 (15%)		
$2 < M_{200}/10^{14}M_{\odot} < 4$	91 (20%)	293 (22%)	
$M_{200}/10^{14}M_{\odot} > 4$	22 (16%)	72 (18%)	38 (25%)

Table 3: Dispersion of $\mu_{200} = M_{\text{lens}}(< \theta_{200})/M_{\text{true}}(< \theta_{200})$ in the raw sample

	$0.2 < z < 0.4$	$0.4 < z < 0.6$	$0.6 < z < 0.8$
$1 < M_{200}/10^{14}M_{\odot} < 2$	(0.69, 0.98)	(0.63, 1.13)	(0.74, 1.74)
$2 < M_{200}/10^{14}M_{\odot} < 4$	(0.55, 0.72)	(0.47, 0.76)	(0.65, 1.28)
$M_{200}/10^{14}M_{\odot} > 4$	(0.45, 0.48)	(0.39, 0.53)	(0.36, 0.77)

For each bin, numbers are given for the noise-free (*left*) and noisy (*right*) cases.

Table 4: Dispersion of $\mu_{200} = M_{\text{lens}}(< \theta_{200})/M_{\text{true}}(< \theta_{200})$ in the clean sample

	$0.2 < z < 0.4$	$0.4 < z < 0.6$	$0.6 < z < 0.8$
$1 < M_{200}/10^{14}M_{\odot} < 2$	(0.60, 0.91)		
$2 < M_{200}/10^{14}M_{\odot} < 4$	(0.44, 0.63)	(0.41, 0.68)	
$M_{200}/10^{14}M_{\odot} > 4$	(0.32, 0.40)	(0.28, 0.42)	(0.25, 0.6)

For each bin, numbers are given for the noise-free (*left*) and noisy (*right*) cases.

Table 5: Mean of $\mu_{200} = M_{\text{lens}}(< \theta_{200})/M_{\text{true}}(< \theta_{200})$ in the clean sample

	$0.2 < z < 0.4$	$0.4 < z < 0.6$	$0.6 < z < 0.8$
$1 < M_{200}/10^{14}M_{\odot} < 2$	(1.02, 1.02)		
$2 < M_{200}/10^{14}M_{\odot} < 4$	(1.00, 0.99)	(1.11, 1.11)	
$M_{200}/10^{14}M_{\odot} > 4$	(1.05, 1.04)	(1.08, 1.08)	(1.14, 1.12)

For each bin, numbers are given for the noise-free (*left*) and noisy (*right*) cases.

Table 6: Skewness of $\mu_{200} = M_{\text{lens}}(< \theta_{200})/M_{\text{true}}(< \theta_{200})$ in the clean sample

	$0.2 < z < 0.4$	$0.4 < z < 0.6$	$0.6 < z < 0.8$
$1 < M_{200}/10^{14}M_{\odot} < 2$	(0.6, 0.16)		
$2 < M_{200}/10^{14}M_{\odot} < 4$	(0.49, 0.32)	(0.56, 0.13)	
$M_{200}/10^{14}M_{\odot} > 4$	(0.60, 0.11)	(0.31, 0.02)	(0.12, 0.07)

For each bin, numbers are given for the noise-free (*left*) and noisy (*right*) cases.

Table 7: Noise-free mean and dispersion for the ratio of the local compensating mass $\Delta M(\theta_{200}, 1.2\theta_{200})$ to the true cluster mass $M(< \theta_{200})$

	$0.2 < z < 0.4$	$0.4 < z < 0.6$	$0.6 < z < 0.8$
$1 < M_{200}/10^{14}M_{\odot} < 2$	(0.25, 0.40)		
$2 < M_{200}/10^{14}M_{\odot} < 4$	(0.21, 0.14)	(0.26, 0.16)	
$M_{200}/10^{14}M_{\odot} > 4$	(0.25, 0.26)	(0.23, 0.29)	(0.18, 0.10)

For each bin, numbers are given for the mean (*left*) and the dispersion (*right*).

Table 8: Mass error dispersions ($\sigma(\mu_{500})$, $\sigma(\mu_{1000})$, $\sigma(\mu_{1500})$) in the clean sample for the noisy case

	$0.2 < z < 0.4$	$0.4 < z < 0.6$	$0.6 < z < 0.8$
$1 < M_{200}/10^{14}M_{\odot} < 2$	(0.53, 0.39, 0.32)		
$2 < M_{200}/10^{14}M_{\odot} < 4$	(0.37, 0.28, 0.22)	(0.41, 0.32, 0.28)	
$M_{200}/10^{14}M_{\odot} > 4$	(0.21, 0.17, 0.13)	(0.29, 0.20, 0.18)	(0.36, 0.28, 0.25)